Active Damping for Dynamic Improvement of Multiple Grid-Tied Virtual Synchronous Generators

Yu, Yun; Chaudhary, Sanjay K.; Tinajero, Gibran David Agundis; Xu, Luona; Vasquez, Juan C.; Guerrero, Josep M.

Published in:
IEEE Transactions on Industrial Electronics

DOI (link to publication from Publisher):
10.1109/TIE.2023.3277082

Publication date:
2024

Document Version
Accepted author manuscript, peer reviewed version

Active Damping for Dynamic Improvement of Multiple Grid-Tied Virtual Synchronous Generators

Yun Yu *Student Member, IEEE*, Sanjay K Chaudhary *Senior Member, IEEE*,
Gibran David Agundis Tinajero *Member, IEEE*, Luona Xu *Student Member, IEEE*,
Juan C. Vasquez *Senior Member, IEEE*, and Josep M. Guerrero *Fellow, IEEE*

***Abstract*—To eliminate low-frequency oscillations, this paper proposes an active-damping method for multiple grid-tied virtual synchronous generators (VSGs) in a power plant. Firstly, using the Lyapunov's indirect method, the damping ratio of multiple VSGs in parallel is analyzed. The average damping ratio reveals that this multi-VSG power plant can be poorly damped in a wide range of inertia and damping settings. Then, self- and mutual-damping controllers are developed to suppress self- and mutually induced low-frequency power oscillations, respectively. For the practical implementation, an adaptive tuning algorithm that enables automatic realization is proposed. Through a reassessment, a remarkable damping-ratio improvement is validated. Moreover, the inertial response improvement is validated by the frequency response analysis. Finally, simulations in Digsilent/PowerFactory and experiments are performed to demonstrate the accuracy of the analyses and the effectiveness of the proposed method.**

***Index Terms*—active damping, power oscillation, small-signal stability, virtual synchronous generator (VSG)**

I. Introduction

TODAY, the virtual synchronous generator (VSG) is drawing more attention for the renewables integration [1]. It provides an explicit emulation of the synchronous machine (SG) swing characteristic [2]; however, this explicit emulation may lead to insufficient damping effects, which in turn causes low-frequency output power oscillations [2], [3].

For the low-frequency power oscillation attenuation, different swing equation modifications have been proposed in the literature. For example, a solution using an additional phase lock loop (PLL) was proposed by Huang et al. in [4]. In spite of the effectiveness in attenuating power oscillations, the PLL-related instability can be problematic in the implementation. Different from the methods using PLLs, in [5] and [6], Dong et al. and Liu et al. proposed damping-correction filters for the grid-tied VSGs. Moreover, the virtual inductance concept was adopted in [7] for the damping purpose. These algorithms are realized by embedding extra filters in the swing equation. Taking both power oscillation attenuation and inertial effect preservation into account, in [8]–[10], Meng et al., Rathnayake et al. and Yu et al. gave distinct solutions. Specifically, Meng et al. proposed a generalized droop method which uses a derivative filter in the active power feedback. To mitigate the noise-amplifying problem of using derivative filters, Rathnayake et al. proposed a generalized VSG design. To decouple the set point tracking and the inertial response, Yu et al. proposed a feedforward control scheme to enable a quantitative and independent tuning of VSG set point tracking and inertial response.

The aforementioned active-damping algorithms were developed on the basis of the fixed-parameter control. Nevertheless, the VSG control parameters are not necessarily constant. For instance, a bang-bang control strategy was proposed in [11] to realize an alternating virtual inertia. A further improvement, which utilizes a combination of adaptive inertia and adaptive damping, was proposed in [12]. With more degrees of freedom involved in the adaptive control law, additional improvements in the VSG dynamic response can be attained. Another group of adaptive methods involves the optimal control. For example, an adaptive algorithm was developed in [13] to guarantee an optimal damping ratio during the transient. Moreover, in [14], an optimal adaptive control was realized using the adaptive dynamic programming, where an optimal regulation problem was formulated to improve the VSG dynamic response.

In these works, the investigation was only made for a single unit, whereas the interactions among different VSG units were disregarded for the analysis benefit. In the case of a multi-VSG system, e.g., a microgrid or a power plant, the effectiveness of the active-damping method for a single VSG may significantly degrade. Considering the operation of a multi-VSG microgrid, Alipoor et al. proposed a real-time tuning algorithm in [15] for ensuring the microgrid global stability. Furthermore, focusing on the VSG parallel operation, a multi-VSG microgrid was investigated in [16], and an inertia control was developed for smoothing the transient. A active-damping strategy combining the virtual damping and virtual reactance was proposed in [17], where the former was used for the oscillation attenuation, and the latter was applied for reducing the oscillation excitation. Another damping strategy using the VSG angular acceleration was developed in [18], where additional frequency and power feedback was included for the active damping. Moreover, Fu et al. proposed decentralized mutual-damping algorithms in [19] and [20] to attenuate the power oscillations in a multi-VSG microgrid. From the existing investigations on the multi-VSG system, it is clear that the investigations mainly focus on the islanded case, and the research on multiple grid-tied VSGs is still limited. In the literature, Qin et al. developed an unified impedance model for analyzing the system oscillation mode of multiple grid-tied VSGs in [21]. Considering the damping of multiple grid-tied VSGs, Sun et al. developed a stabilizer by linking the angular frequency deviation with the excitation in [22]. In addition, VSG tuning guidelines were presented in [23] for the stable operation of a multi-VSG power plant.

A technical future summary of the active-damping methods is given in Table I. Clearly, more investigations are needed

Table I
TECHNICAL FEATURES OF EXISTING ACTIVE-DAMPING METHODS

Reference	VSG	Grid-tied	Islanded	Inertial response	Tuning	Reference	VSG	Grid-tied	Islanded	Inertial response	Tuning
[4]–[7]	1	✓	✗	Disregarded	Manual	[15]	3	✗	✓	Disregarded	Optimization
[8], [9]	1	✓	✗	Involved	Manual	[16]	2	✗	✓	Involved	Manual
[10]	1	✓	✗	Involved	Calculation	[17], [18]	2	✗	✓	Involved	Manual
[11], [13]	1	✓	✗	Disregarded	Manual	[19]	4	✗	✓	Involved	Manual
[14]	1	✓	✗	Disregarded	Data-driven	[20]	4	✗	✓	Involved	Manual
[12]	1	✗	✓	Involved	Manual	[22]	3	✓	✗	Disregarded	Optimization

for multiple VSGs, especially in the grid-tied case. Therefore, an active-damping strategy, which consists of both self- and mutual-damping controllers, is developed in this paper. The technical contributions are summarized as follows:

1) Damping characteristics of the parallel operation of multiple grid-tied VSGs in a power plant are analyzed via a full-order model and the Lyapunov's indirect method.
2) An active-damping method has been proposed for the parallel operation of multiple grid-tied VSGs. This method enables an effective attenuation of both self- and mutually induced low-frequency power oscillations, which leads to smooth and decoupled transients.
3) Compared with the existing active-damping methods, by applying the proposed controllers, the inertial response of multiple parallel grid-tied VSGs can be better enhanced for supporting the grid frequency.
4) Quantitative tuning guidelines are derived. The proposed tuning algorithm is designed to be implemented online to adapt to the system setting change, which leads to more flexibility in practice.

This paper is arranged as follows: The system is introduced in Section II. In Section III, a damping-ratio assessment is conducted, and the proposed active-damping method is given. In Section IV, the evaluations are given. Finally, the conclusion and future work are summarized in Section V and VI.

II. SYSTEM DESCRIPTION

A. Circuit Topology

A system equivalent representation is shown in Fig. 1. Here, R_{fn}, L_{fn} and C_{fn} are resistance, inductance and capacitance of the nth VSG output filter, where $n = 1, 2, \ldots, N$, and N is the VSG number. R_{ln} and L_{ln} are equivalent resistance and inductance between the filter and the point of common coupling (PCC). Considering that the investigation on the oscillation focuses on the power plant, the external electrical networks are simplified into grid-side resistance and inductance, i.e., R_g and L_g. P_n and Q_n are active and reactive power of the

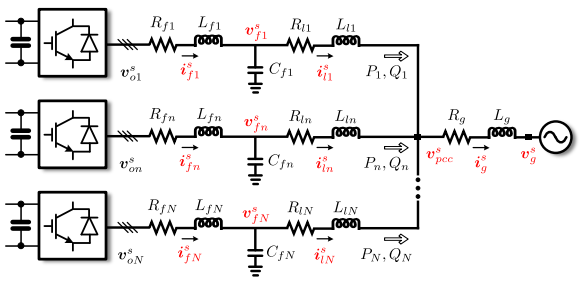

Figure 1. Multiple parallel grid-tied VSGs in a power plant.

nth VSG. The boldface letters with the superscript s denote current and voltage vectors in the nth $\alpha\beta$ frame, such as $\boldsymbol{v}^s_{on}$, $\boldsymbol{i}^s_{fn}$, $\boldsymbol{v}^s_{fn}$, $\boldsymbol{i}^s_{ln}$, $\boldsymbol{v}^s_{pcc}$, $\boldsymbol{i}^s_g$ and $\boldsymbol{v}^s_g$. Vectors in the nth dq frame are written as $\boldsymbol{v}_{on}$, $\boldsymbol{i}_{fn}$, $\boldsymbol{v}_{fn}$, $\boldsymbol{i}_{ln}$ and $\boldsymbol{v}_{pccn}$, and vectors in the grid DQ frame are written as $\boldsymbol{I}_{ln}$, $\boldsymbol{V}_{pcc}$, $\boldsymbol{I}_g$ and $\boldsymbol{V}_g$.

B. Circuit Model

Referring to Fig. 1, the circuits between the nth inverter and the PCC are modeled in the nth dq frame as follows:

$$L_{fn}\dot{\boldsymbol{i}}_{fn} = \boldsymbol{v}_{on} - (R_{fn} + j\omega_n L_{fn})\,\boldsymbol{i}_{fn} - \boldsymbol{v}_{fn} \tag{1}$$

$$C_{fn}\dot{\boldsymbol{v}}_{fn} = \boldsymbol{i}_{fn} - j\omega_n C_{fn}\boldsymbol{v}_{fn} - \boldsymbol{i}_{ln} \tag{2}$$

$$L_{ln}\dot{\boldsymbol{i}}_{ln} = \boldsymbol{v}_{fn} - (R_{ln} + j\omega_n L_{ln})\,\boldsymbol{i}_{ln} - \boldsymbol{v}_{pccn} \tag{3}$$

where ω_n is the the nth VSG angular frequency.

Then, the grid DQ frame is taken as the common coordinate frame, and its angular frequency ω_g is considered as a constant. Let δ_n denote the angle difference between the nth VSG and grid coordinates, we have $\delta_n = \theta_n - \theta_g$, where $\dot{\theta}_n = \omega_n$ and $\dot{\theta}_g = \omega_g$. Afterwards, the coordinate transformations between the nth dq and DQ frames can be defined as follows:

$$\boldsymbol{v}_{pccn} = e^{-j\delta_n}\boldsymbol{V}_{pcc},\ \boldsymbol{I}_{ln} = e^{j\delta_n}\boldsymbol{i}_{ln}. \tag{4}$$

Referring to Fig. 1, the dynamic of the grid-side transmission line is modeled in the DQ frame as

$$L_g\dot{\boldsymbol{I}}_g = \boldsymbol{V}_{pcc} - (R_g + j\omega_g L_g)\,\boldsymbol{I}_g - \boldsymbol{V}_g. \tag{5}$$

C. VSG Control Basis

The control scheme of each inverter is illustrated in Fig. 2. It includes the active power control (APC), reactive power control (RPC), virtual impedance, inner current-voltage control. The instantaneous power of the nth VSG is

$$P_n + jQ_n = 3\boldsymbol{v}_{fn}\bar{\boldsymbol{i}}_{ln}/2 \tag{6}$$

where $\bar{\boldsymbol{i}}_{ln}$ is the conjugate vector of $\boldsymbol{i}_{ln}$.

For the nth VSG, the APC is written as

$$M_n\dot{\omega}_n = P^*_n - P_n - D_n\,(\omega_n - \omega_0) \tag{7}$$

where P^*_n is the active power set point; M_n denotes the virtual inertia that is equal to $2S_{\text{base}}H_n/\omega_0$, where S_{base}, H_n, and ω_0 are rated power, inertia constant, and nominal frequency, respectively; D_n denotes the VSG damping factor.

For the nth VSG, the RPC is formulated as

$$V^*_n = m_{pn}(Q^*_n - Q_n) + m_{in}x_{Vn} + V_0 \tag{8}$$

where Q^*_n is the reactive power set point. m_{pn} and m_{in} are proportional and integral control gains; V_0 and V^*_n are nominal

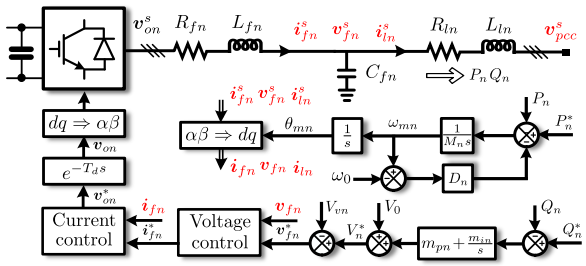

Figure 2. The VSG with a cascaded current-voltage control.

voltage amplitude and nth VSG voltage amplitude set point; x_{Vn} is a state variable, whose derivative is $\dot{x}_{Vn} = Q^*_n - Q_n$.

The virtual impedance is included in the control as

$$\boldsymbol{v}^*_{fn} = V^*_n - \boldsymbol{i}_{ln}\left(R_{vn} + jX_{vn}\right) \tag{9}$$

where $\boldsymbol{v}^*_{fn}$ is the voltage-control set point; R_{vn} is the virtual resistance, and X_{vn} denotes the virtual inductance.

The dq-frame voltage and current controls yield

$$\boldsymbol{i}^*_{fn} = k_{pn}(\boldsymbol{v}^*_{fn} - \boldsymbol{v}_{fn}) + k_{in}\boldsymbol{\gamma}_n + j\omega_n C_{fn}\boldsymbol{v}_{fn} \tag{10}$$

$$\boldsymbol{v}^*_{on} = l_{pn}(\boldsymbol{i}^*_{fn} - \boldsymbol{i}_{fn}) + l_{in}\boldsymbol{\zeta}_n + j\omega_n L_{fn}\boldsymbol{i}_{fn} + \boldsymbol{v}_{fn} \tag{11}$$

where $\boldsymbol{i}^*_{fn}$ and $\boldsymbol{v}^*_{on}$ are current-control and inverter-output set points. k_{pn}, k_{in}, l_{pn}, and l_{in} are proportional and integral gains of the voltage and current control, respectively. $\boldsymbol{\gamma}_n$ and $\boldsymbol{\zeta}_n$ are two state variables, and their derivatives are defined as

$$\dot{\boldsymbol{\gamma}}_n = \boldsymbol{v}^*_{fn} - \boldsymbol{v}_{fn},\ \dot{\boldsymbol{\zeta}}_n = \boldsymbol{i}^*_{fn} - \boldsymbol{i}_{fn}. \tag{12}$$

The effect of the control latency is formulated as

$$\dot{\boldsymbol{v}}_{on} \approx \left(\boldsymbol{v}^*_{on} - \boldsymbol{v}_{on}\right)(1.5T_c)^{-1} \tag{13}$$

where T_c is the time period for the sampling and control.

III. Damping of Multiple Grid-Tied VSGs

A. Damping-Ratio Assessment

Using equations (1) to (13), the multiple grid-tied VSGs can be represented by a set of differential equations as $\dot{\mathbf{x}} = \mathbf{f}(\mathbf{x})$. The vector function $\mathbf{f}(\mathbf{x})$ is formulated as

$$\mathbf{f}(\mathbf{x}) = \left[f_1(x_1, \ldots, x_S) \ldots f_S(x_1, \ldots, x_S)\right]^{\mathrm{T}} \tag{14}$$

where S is the number of states. Here, it is equal to $15N+2$. $f_1(x_1, \ldots, x_S)$ to $f_S(x_1, \ldots, x_S)$ denote components of the vector function $\mathbf{f}(\mathbf{x})$, and x_1 to x_S are state variables. The state matrix $\mathbf{x}$ is expressed as

$$\begin{aligned}\mathbf{x} &= \left[\mathbf{x}_{cir1}\ \mathbf{x}_{vsg1}\ \mathbf{x}_{cir2}\ \mathbf{x}_{vsg1}\ \ldots\ \mathbf{x}_{cirN}\ \mathbf{x}_{vsgN}\ \mathbf{x}_{Ig}\right]^{\mathrm{T}} \\ &\triangleq \left[x_1\ x_2\ \ldots\ x_S\right]^{\mathrm{T}}\end{aligned} \tag{15}$$

where $\mathbf{x}_{Ig}$, $\mathbf{x}_{cirn}$, and $\mathbf{x}_{vsgn}$ are

$$\mathbf{x}_{Ig} = \left[I_{gD}\ I_{gQ}\right],\ \mathbf{x}_{cirn} = \left[i_{fdn}\ i_{fqn}\ v_{fdn}\ v_{fqn}\ i_{ldn}\ i_{lqn}\right],$$
$$\mathbf{x}_{vsgn} = \left[v_{odn}\ v_{oqn}\ \gamma_{dn}\ \gamma_{qn}\ \zeta_{dn}\ \zeta_{qn}\ x_{Vn}\ \omega_n\ \delta_n\right].$$

From (14), the Jacobian matrix $\mathbf{J}$ can be obtained as

$$\mathbf{J} = \left[\partial\mathbf{f}/\partial x_1\ \partial\mathbf{f}/\partial x_2\ \ldots\ \partial\mathbf{f}/\partial x_S\right]. \tag{16}$$

Then, the damping ratio can be estimated via the eigenvalues λ_i of the matrix $\mathbf{J}$, where $i = 1, 2, \ldots, S$.

Table II
Circuit Parameters

Symbol	Values	Symbol	Values	Symbol	Values
S_{base}	1 MVA	V_{line}	690 V	R_{fn}	0.006 p.u.
L_{fn}	0.12 p.u.	C_{fn}	0.2 p.u.	R_{ln}	0.01 p.u.
L_{ln}	0.1 p.u.	R_g	0.007 p.u.	L_g	0.066 p.u.

Table III
VSG Control Parameters

Symbol	Values	Symbol	Values	Symbol	Values
l_{pn}	0.64 p.u.	l_{in}	38.59 p.u.	k_{pn}	0.25 p.u.
k_{in}	52.37 p.u.	R_{vn}	0.013 p.u.	X_{vn}	0.22 p.u.
T_c	0.0005 s	H_n	15 s	D_n	10 p.u.
m_{pn}	1.15 p.u.	m_{in}	3 p.u.	V_0	563 V

The circuit data are given in Table II, and the VSG control parameters are presented in Table III. The bandwidths of the voltage and current control are adjusted to 135 Hz and 225 Hz. The resulting phase margins are 45° and 49°. The equivalent grid-side impedance is adjusted by the virtual impedance to be mainly inductive. H_n and D_n correspond to 15 s inertia constant and 10% static droop. Regarding the RPC, its bandwidth is adjust to the same level as the APC [3]. For the damping-ratio assessment and the active-damping strategy development, the dominant oscillation modes are calculated under different N. Here, the eigenvalues with a real part greater than -2 are taken as dominant. The remaining eigenvalues are so far that their effects can be disregarded.

Table IV
VSG number and dominant oscillation modes

$N=1$	$N=2$	$N=3$	$N=4$	$N=5$
$-0.38\pm j5.3$	$-0.3\pm j4.8$	$-0.26\pm j4.3$	$-0.25\pm j3.8$	$-0.25\pm j3.3$
NA	$-0.52\pm j5.9$	$-0.52\pm j5.8$	$-0.51\pm j5.7$	$-0.51\pm j5.5$
NA	$-1.55\pm j35$	$-1.47\pm j34$	$-1.34\pm j34$	$-1.14\pm j34$

As depicted in Table IV, when $1 < N \leq 5$, there are three dominant oscillation modes. Roughly, they tend to be settled when $3 \leq N$. As the main scope of this paper is to develop an active-damping method for the dynamic improvement rather than maximizing the number of VSGs, the number of VSGs is thus set to 3 in this paper as a generalized case.

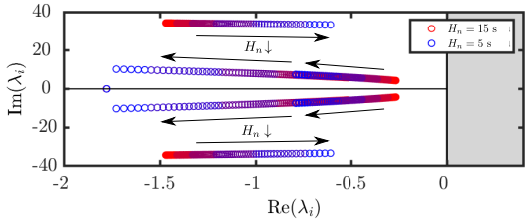

Figure 3. Dominant eigenvalue loci when $D_n = 10$ p.u., and $H_n \in [5, 15]$ s.

1) Same H_n and D_n: In this scenario, H_n and D_n are set to the same, the system dominant eigenvalues are shown in Fig. 3. When $D_n = 10$ p.u. and $H_n = 15$ s, there are poorly-damped complex eigenvalues which are close to the imaginary axis. It indicates that the system has oscillatory responses under perturbations. Then, an average damping ratio ζ_{av} is calculated

in the range of $H_n \in [5, 15]$ s and $D_n \in [10, 50]$ p.u. as

$$\zeta_{av} = \sum_{l=1}^{L} \frac{-Real(\lambda_l)}{L\sqrt{Real(\lambda_l)^2 + Imag(\lambda_l)^2}} \tag{17}$$

where L is the number of the dominant eigenvalues.

The results are shown in Fig. 4. It is clear that, on the most of the H_n-D_n parameter plane, the average damping ratio is less than 0.2. Only when the H_n is small and D_n is large enough, it increases slightly to 0.23.

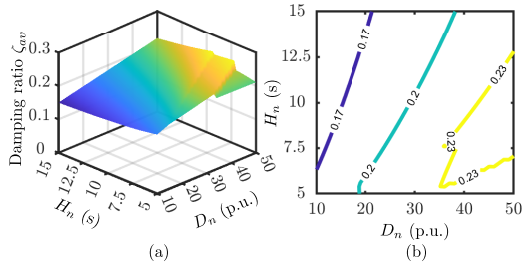

Figure 4. Average damping ratio in the range of $H_n \in [5, 15]$ s and $D_n \in [10, 50]$ p.u.. (a) damping ratio (b) damping ratio contour lines.

2) Different H_n and D_n: In this scenario, the parameters of two VSGs are fixed, for example, $H_2 = 11.25$ s, $H_3 = 15$ s, $D_2 = 15$ p.u. and $D_3 = 10$ p.u.. Then, only the parameters of one VSG are changed.

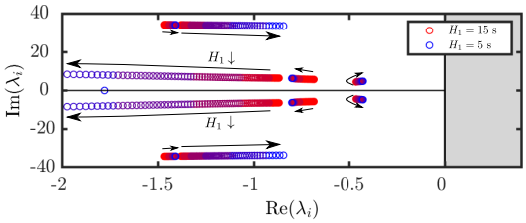

Figure 5. Dominant eigenvalue loci when $D_1 = 20$ p.u., and $H_1 \in [5, 15]$ s.

As shown in Fig. 5, when $D_1 = 20$ p.u., and H_1 varies from 5 s to 15 s, some dominant eigenvalues move toward the left-side locations that has higher damping ratios. Meanwhile, two poorly-damped complex eigenvalues barely move. The average damping ratio is always less than 0.3. On the most of the H_1-D_1 parameter plane, it is less than 0.26, as shown in Fig. 6.

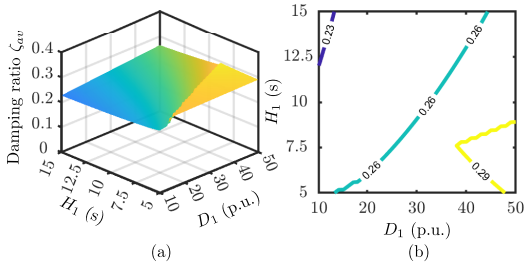

Figure 6. Average damping ratio in the range of $H_1 \in [5, 15]$ s and $D_1 \in [10, 50]$ p.u.. (a) damping ratio (b) damping ratio contour lines.

From the above analyses, it can be derived that the multiple grid-tied VSGs can be poorly-damped, even when parameters H_n and D_n are changed in a wide range. Consequently, in the case of a perturbation, e.g., set point change, frequency or voltage variation, the output power may contain oscillations. Normally, a larger D_n will lead to a better damping effect, as depicted in Figs. 5 and 6; however, it also affects the droop factor that determines the inverter primary-frequency support.

B. Active-Damping Algorithm

Considering the previous results, an algorithm is proposed to improve the damping ratio without changing D_n.

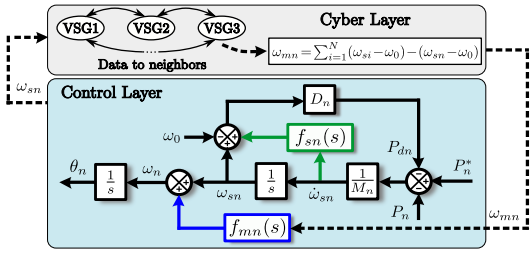

Figure 7. APC with the proposed active-damping algorithm.

As shown in Fig. 7, the proposed active-damping algorithm consists of the self-damping controller $f_{sn}(s)$ and the mutual-damping controller $f_{mn}(s)$. Controller $f_{sn}(s)$ limits the self-induced oscillations. Simultaneously, using the communication links of the upper layer, controller $f_{mn}(s)$ attenuates the mutually induced oscillations. The resulting APC yields

$$\omega_n = \omega_{sn} + \omega_{mn} f_{mn}(s) \tag{18}$$

$$M_n \dot{\omega}_{sn} = P_n^* - P_n - D_n \left[\omega_{sn} - \omega_0 + f_{sn}(s)\dot{\omega}_{sn}\right] \tag{19}$$

where $\omega_{mn} = \sum_{i=1}^{N}(\omega_{si} - \omega_0) - (\omega_{sn} - \omega_0)$ is the frequency variation fed into the mutual-damping controller $f_{mn}(s)$; ω_{sn} denotes the angular frequency that is generated by the swing equation and the self-damping controller $f_{sn}(s)$.

C. Self-Damping Controller $f_{sn}(s)$

The grid is first assumed to be an infinite bus, and the VSG is simplified as a voltage source. The voltage amplitudes of the grid and VSG are assumed to be V_0. The active power of each VSG is then written as

$$P_n = \frac{3V_0^2}{2X_{en}} \sin\delta_n \approx \frac{3V_0^2}{2X_{en}} \delta_n \tag{20}$$

where $X_{en} = \omega_0 (L_g + L_{ln}) + X_{vn}$ is the output impedance. As L_g may change depending on the operating condition, To obtain X_{en}, an online impedance detection can be applied.

Neglecting the mutual-damping controller $f_{mn}(s)$, we have $\omega_n = \omega_{sn}$. Afterwards, using (20) and (19), the APC loop in the sense of small signal, i.e., $\Delta P_n / \Delta P_n^*$, is derived as

$$f_{pn}(s) = \frac{3V_0^2}{2X_{en}\left[M_n s^2 + D_n f_{sn}(s) s^2 + D_n s\right] + 3V_0^2}. \tag{21}$$

Here, one of the self-damping controller $f_{sn}(s)$ design criteria is to minimize the magnitude of $f_{pn}(s)$ at the oscillation frequency without degrading the APC bandwidth. Meanwhile, the magnitude of $f_{pn}(s)$ within the bandwidth should be small enough. For this, an objective function is defined as follows:

$$min \qquad |f_{pn}(j\omega_{on})| \tag{22}$$

$$s.t. \qquad 20\log_{10}|f_{pn}(j\omega_{cn})| = -3 \text{ dB} \tag{23}$$

$$\forall\omega \in [0, \omega_{cn}] \quad 20\log_{10}|f_{pn}(j\omega)| \leq 3 \text{ dB} \tag{24}$$

where ω_{on} is the oscillation frequency, and ω_{cn} is the the cut-off frequency; ω denotes any frequency between 0 and ω_{cn}.

1) $f_{sn}(s) = 0$: In this scenario, $f_{sn}(s)$ is first set to 0, which corresponds to the VSG without the proposed damping algorithm. Then, from (21), it can be derived that $f_{pn}(s)$ has two complex eigenvalues, the natural frequency of which is the oscillation frequency ω_{on}, and it is expressed as

$$\omega_{on} = \sqrt{\frac{3V_0^2}{2X_{en}M_n}}. \tag{25}$$

Assuming that ω_{cn} is the cut-off frequency of the original APC loop which is applied without $f_{sn}(s)$, and substituting $s = j\omega_{cn}$ into (21), we have

$$\left| \frac{3V_0^2}{2X_{en}\left(jD_n\omega_{cn} - M_n\omega_{cn}^2\right) + 3V_0^2} \right| = 0.708 \tag{26}$$

where $0.708 \approx 10^{\frac{-3}{20}}$. Using the $fsolve$ function in MATLAB, the solution for (26), namely ω_{cn}, can be easily obtained.

2) $f_{sn}(s) \neq 0$: Due to the integrator in the swing equation, the phase difference between ω_{sn} and $\dot{\omega}_{sn}$ is $\pi/2$. Thus, when $\dot{\omega}_{sn}$ is utilized to generate the additional damping term, it is preferable to let the output of $f_{sn}(s)$ has a $\pi/2$ phase delay at the frequency of oscillation ω_{on}. In this manner, the damping power P_{dn} in Fig. 7 still has the similar oscillatory pattern as ω_{sn}. Then, P_{dn} can be enlarged properly during the transient process, and it is only governed by the damping factor D_n when VSGs come to the steady state, i.e., $\dot{\omega}_{sn} = 0$. To achieve this, the controller $f_{sn}(s)$ is proposed as follows:

$$f_{sn}(s) = \frac{k_{sn}T_{sn}\omega_{dn}^2}{s^2 + T_{sn}\omega_{dn}s + \omega_{dn}^2} \tag{27}$$

where k_{sn} and T_{sn} are parameters for adjusting the controller gain and bandwidth; ω_{dn} denotes the center frequency where the sinusoidal signal has a $\pi/2$ phase delay, and it is is set to the same value as (25), i.e., $\omega_{dn} = \omega_{on}$.

Subsequently, substituting ω_{cn} into (23), an equality constraint is obtained. Regarding the inequality constraint (24), there are infinite points between 0 and ω_{cn}. In order to solve the optimization problem, several frequencies are selection for the frequency ω in (24), e.g., $\omega = 0.1\omega_{sn}, 0.2\omega_{sn}, \ldots, 0.9\omega_{sn}$. Then, using (22), (23), and (24), and applying the $fmincon$ function in MATLAB, k_{sn} and T_{sn} in (27) are solved.

To reflect the impact of $f_{sn}(s)$ on the VSG inertial response. The small signal model that indicates the inertial response is derived from (19) as [8], [9]

$$f_{in}(s) = -\frac{1}{\left[M_n + D_n f_{sn}(s)\right]s + D_n}. \tag{28}$$

From (28), it is clear that $D_n f_{sn}(s)$ works as an additional frequency-dependent inertia term, and it contributes to enhancing the virtual inertia mainly in the low frequency range since (27) inherently exhibits a low-pass characteristic. In this sense, applying $f_{sn}(s)$ fits the aim of preserving the inertial response.

D. Mutual-Damping Controller

The mutually induced power oscillations are caused by the interactions among parallel VSGs. Due to the existence of the grid impedance, once there are active power variations in one VSG, phase angle changes of the grid voltage are introduced in the other VSGs dq coordinates. Subsequently, the mutually induced power oscillations at different oscillation frequencies ω_{on} are triggered. To compensate these phase angle changes, the mutual-damping controller $f_{mn}(s)$ is applied as

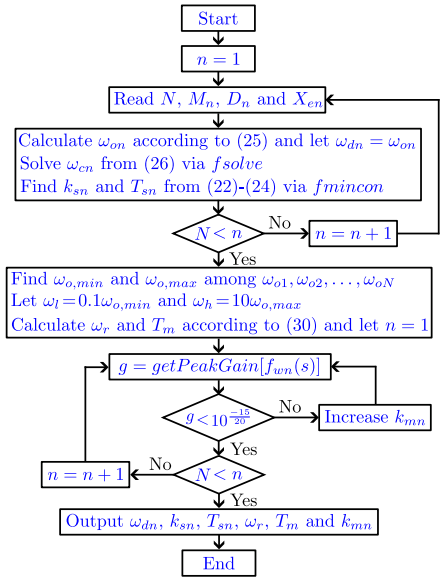

Figure 8. Flowchart of the tuning processes.

$$f_{mn}(s) = \frac{k_{mn}\omega_r s}{T_m s^2 + \omega_r s + T_m\omega_r^2} \tag{29}$$

where ω_r denotes the center frequency, where $f_{mn}(s)$ has the highest gain k_{mn}, and T_m is the parameter for adjusting the filter selectivity. ω_r and T_m can be written as

$$\omega_r = \sqrt{\omega_l\omega_h},\ T_m = \frac{\sqrt{\omega_l\omega_h}}{\omega_h - \omega_l} \tag{30}$$

where ω_l and ω_h are filter lower and upper cut-off frequencies.

In order to let $f_{mn}(s)$ have enough gain for all the mutually induced oscillations, we should have

$$\forall n \in [1, N] \quad \omega_l \ll \omega_{on} \ll \omega_h. \tag{31}$$

For simplicity, ω_l and ω_h can be directly set to $0.1\omega_{o,min}$ and $10\omega_{o,max}$, where $\omega_{o,min}$ and $\omega_{o,max}$ are minimum and maximum values of ω_{on}. In this way, only the k_{mn} is left for tuning. Then, substituting (20) into (18) and (19), the small-signal model of $\Delta\omega_{sn}$ over $\Delta\omega_{mn}$ is derived as

$$f_{\omega n}(s) = \frac{-3V_0^2 f_{mn}(s)s}{2X_{en}\left(M_n s + D_n f_{sn}(s)s + D_n\right) + 3V_0^2 s}. \tag{32}$$

Since $\Delta\omega_{mn}$ just compensates the disturbances, it should not affect the regulation of the swing equation and the self-damping controller $f_{sn}(s)$. In another word, $f_{mn}(s)$ should be designed to let $\Delta\omega_{mn}$ have almost no impact on $\Delta\omega_{sn}$. Thus, the magnitude of $f_{\omega n}(s)$ should be much smaller than unity in the entire frequency range, and it is formulated as

$$\forall\omega \in [0, \infty] \quad 20\log_{10}\left|f_{\omega n}(j\omega)\right| \ll 0 \text{ dB}. \tag{33}$$

For the benefit of the controller design, the maximum value of $20\log_{10}\left|f_{\omega n}(j\omega)\right|$ is set to -15 dB to ensure (33). Then, with the help of the $getPeakGain$ function in MATLAB, the k_{mn}, which corresponds to this magnitude, can be estimated by iterations. The entire design is then illustrated by Fig. 8.

IV. Evaluations

To validate the proposed method, a study case with the lowest damping ratio in Figs. 4 and 6 is adopted: $H_n = 15$ s and $D_n = 10$ p.u.. Then, using the proposed tuning algorithm, the parameters of controllers $f_{sn}(s)$ and $f_{mn}(s)$ are obtained as shown in Table V. As the communication in practice may cause additional latency, the time delay T_{com} that origins from the communication among multiple VSGs is set to 25 ms.

Table V
Parameters of controllers $f_{sn}(s)$ and $f_{mn}(s)$

VSG	ω_{dn}	k_{sn}	T_{sn}	ω_r	T_m	k_{mn}
1∼3	5.21 rad/s	2.27	3.78	5.21 rad/s	0.21	0.185

A. Damping-Ratio Reassessment

Replacing (7) with (18) and (19), substituting (27) and (29), approximating the communication latency as $(T_{com}s + 1)^{-1}$, the system model (14) is reformulated as $\dot{\mathbf{x}}_{ad} = \mathbf{g}(\mathbf{x}_{ad})$, and the new vector function $\mathbf{g}(\mathbf{x}_{ad})$ is written as

$$\mathbf{g}(\mathbf{x}_{ad}) = [g_1(x_1, \ldots, x_S), \ldots, g_S(x_1, \ldots, x_S)]^{\mathrm{T}} \qquad (34)$$

where g_1 to g_S are components of the vector function $\mathbf{g}(\mathbf{x}_{ad})$; $\mathbf{x}_{ad}$ denotes the state vector with extended state variables, and x_1 to x_S are state variables. Here, $S = 20N + 2$.

Using the same settings in Section III-A, an extended Jacobian matrix $\mathbf{J}_{ad}$ is obtained. New eigenvalues are subsequently calculated for the comparison. As shown clearly in Fig. 9 (a), when the proposed self-damping controller $f_{sn}(s)$ is applied for each VSG, the most dominant oscillation modes have been eliminated. The average damping ratio ζ_{av} in (17) increases from 0.15 to 0.45. In this manner, the majority of output power oscillations can be well attenuated. Then, the mutual-damping controller $f_{mn}(s)$ is applied. As depicted in Fig. 9 (b), when both $f_{sn}(s)$ and $f_{mn}(s)$ are applied, real eigenvalues will shift toward the imaginary axis, and ζ_{av} increases to 0.57.

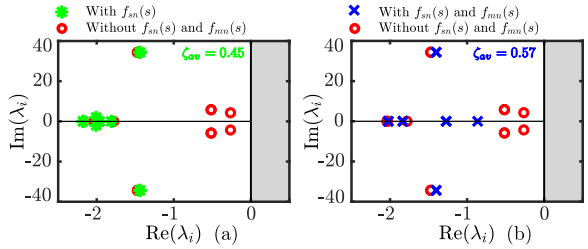

Figure 9. Dominant eigenvalues with and without the proposed method: (a) With only $f_{sn}(s)$; (b) With both $f_{sn}(s)$ and $f_{mn}(s)$.

The impact of the grid impedance and communication delay variations on the proposed active-damping method is verified. As depicted in Fig. 10 (a), when that the real grid inductance varies from 0.6 to 1.4 times the estimation value L_g, the dominant eigenvalues only change slightly. The well-damped performance remains. When the communication delay changes from 0 to 75 ms, it can be observed in Fig. 10 (b) that, the eigenvalues barely move. Clearly, the proposed active-damping method provides enough robustness against the grid impedance and communication delay variations.

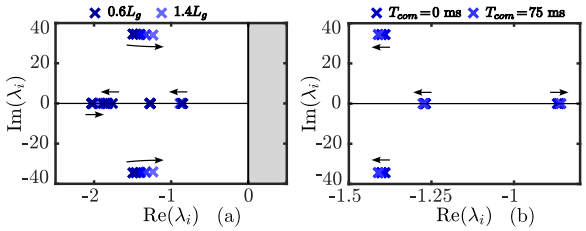

Figure 10. Dominant eigenvalues under grid impedance and communication delay variations: (a) The real grid inductance varies from $0.6L_g$ to $1.4L_g$; (b) The communication delay varies from 0 to 75 ms.

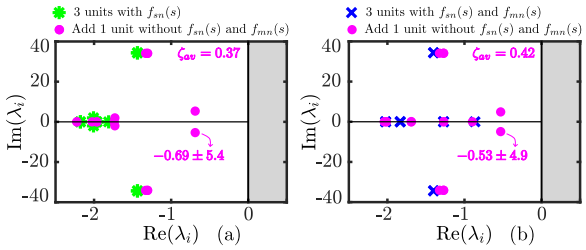

Figure 11. Dominant eigenvalues with and without one extra VSG: (a) Three VSGs with only $f_{sn}(s)$; (b) Three VSGs with both $f_{sn}(s)$ and $f_{mn}(s)$.

In order to reflect the impact of an uncertain VSG number, the proposed controllers are first designed based on $N = 3$. An extra VSG is then added without being involved in the proposed active-damping method. The dominant eigenvalues are depicted in Fig. 11. It is clear that, newly-added oscillation modes become the most dominant, but the well-damped performance of the original VSGs remains the same.

B. Simulation Validation

Subsequently, EMT simulations in Digsilent/PowerFactory are conducted. The system as Fig. 1 is implemented, and the parameters given in Table II, III, and V are adopted. As shown in Figs.12 (a) and (b), without the proposed method, VSG angular frequency ω_n and output power P_n oscillate under power set point changes ($\Delta P_n^* = -0.2$ p.u.). With the self-damping controller $f_{sn}(s)$, those oscillations are effectively attenuated, whereas the interactions among VSGs still exist, as depicted in Figs. 12 (c) and (d). When the mutual-damping controller $f_{mn}(s)$ is applied, both oscillations and slight interactions are well attenuated. In this manner, VSG output

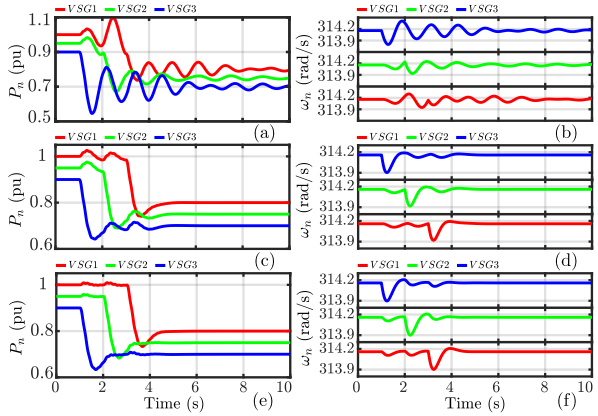

Figure 12. VSG output power P_n and angular frequency ω_n under set point changes ($\Delta P_n^* = -0.2$ p.u.). Without the proposed method: (a) and (b); With $f_{sn}(s)$: (c) and (d); With $f_{sn}(s)$ and $f_{mn}(s)$: (e) and (f).

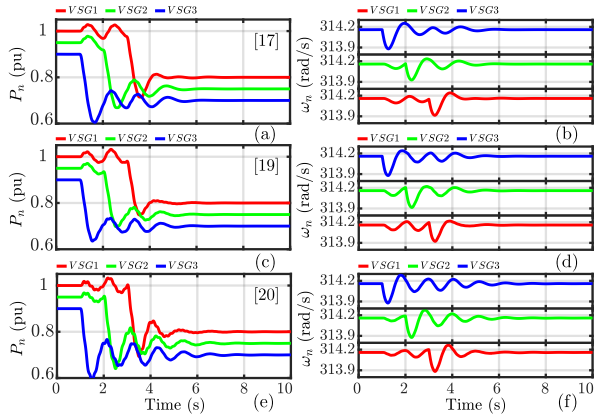

Figure 13. VSG output power P_n and angular frequency ω_n under set point changes ($\Delta P_n^* = -0.2$ p.u.). With the method in [17]: (a) and (b); With the method in [19]: (c) and (d); With the method in [22]: (e) and (f).

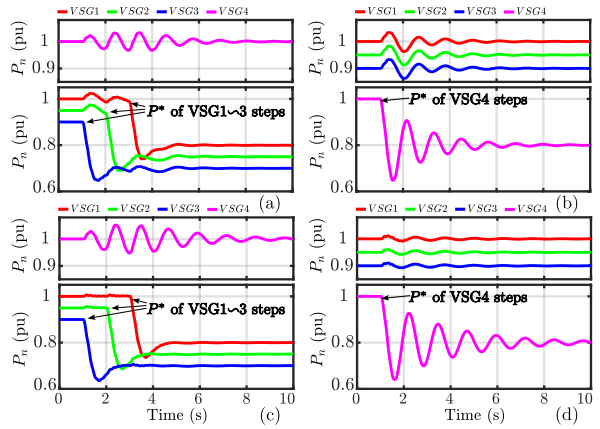

Figure 14. VSG output power P_n and angular frequency ω_n under set point changes ($\Delta P_n^* = -0.2$ p.u.). With $f_{sn}(s)$: (a) Set points of VSG1 to VSG3 change; (b) The set point of VSG4 changes; With $f_{sn}(s)$ and $f_{mn}(s)$: (c) Set points of VSG1 to VSG3 change; (d)The set point of VSG4 changes.

powers are smooth and decoupled from each other, as depicted in Fig. 12 (e). Although these interactions are not intensive to threaten the system stability significantly, for a better output power quality, it is preferable to let VSGs output decoupled. The active-damping methods in [17], [19] and [22] are adopted for the comparison, and the APC bandwidth is adjusted to the same level for the fairness. As depicted in Fig. 13, from the response of VSG1, it is clear that these methods improve the damping ratio well. However, without taking interactions into consideration, these methods provide less effectiveness in attenuating the oscillations caused by the interaction, as shown in the responses of VSG2 and VSG3.

When an extra VSG without the proposed damping method, i.e., VSG4, is applied, as shown in Fig. 14, its output inevitably oscillates, and the oscillation frequency is roughly the same as the dominant oscillation mode shown in Figs. 11 (a) and (b). Regarding VSG1-3, as shown in Figs. 14 (a) and (b), when VSG1-3 are applied with the self-damping controller $f_{sn}(s)$, there are still slight oscillations that are caused by the interactions. In comparison, as shown in Figs. 14 (c) and (d), once the mutual-damping controller $f_{mn}(s)$ is applied, those slight oscillations are attenuated. The output of VSG1-3 can be regulated well without being affected by the VSG4.

Table VI
SG AND ELECTRICAL NETWORK DATA

Variable	Symbol	Values
Inertia constant	H_G	15 s
Damping factor	D_G	1 p.u.
Droop constant	R_G	0.05 p.u.
Speed governor coefficient	T_G	0.1 s
Turbine HP coefficient	F_{HP}	0.3
Time constant of reheater	T_{RH}	7 s
Time constant of main inlet volumes	T_{CH}	0.2 s
Line impedance	X_1,X_2, and X_2	0.32 p.u.
Line impedance	X_4	0.065 p.u.

C. Compatibility With SG

For an impact analysis, the power-frequency dynamic of a system shown in Fig. 15 is investigated. Here, one area is a VSG-based power plant, and another is the conventional SG.

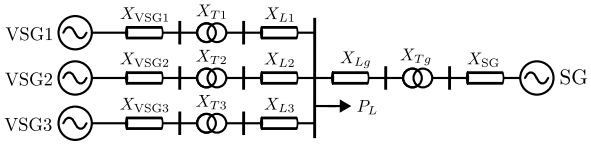

Figure 15. Equivalent electrical diagram of a two-area system.

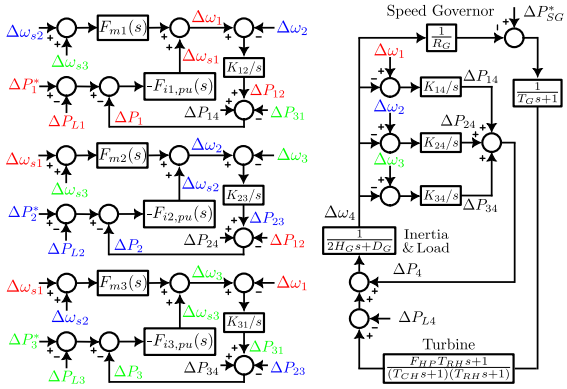

Figure 16. Block diagram of the two-area system.

The simplified block diagram of the system is presented in Fig. 16, where ΔP_{L1}, ΔP_{L2}, ΔP_{L3} and ΔP_{L4} denote load powers supplied by the VSGs and SG, and they are written as

$$\Delta P_{Li} = \frac{1}{X_i \sum_{j=1}^{4} \frac{1}{X_j}} \Delta P_L \tag{35}$$

where ΔP_L is the total load power, $i = 1, 2, 3, 4$, and

$$X_1 = X_{\text{VSG1}} + X_{T1} + X_{L1}, X_2 = X_{\text{VSG2}} + X_{T2} + X_{L2},$$
$$X_3 = X_{\text{VSG3}} + X_{T3} + X_{L3}, X_4 = X_{\text{SG}} + X_{Tg} + X_{Lg}.$$

In addition, in Fig. 16, $F_{mn}(s)$ and $F_{in,pu}(s)$ are

$$F_{mn}(s) = \frac{f_{mn}(s)}{T_{com}s + 1}, \; F_{in,pu}(s) = \frac{\omega_0 f_{in}(s)}{S_{base}} \tag{37}$$

where $n = 1, 2, 3$; K_{12}, K_{23}, K_{31}, K_{14}, K_{24} and K_{34} are

$$K_{12} = \frac{K}{X_1 + X_2}, \; K_{23} = \frac{K}{X_2 + X_3}, \; K_{31} = \frac{K}{X_3 + X_1},$$
$$K_{14} = \frac{K}{X_1 + X_4}, \; K_{24} = \frac{K}{X_2 + X_4}, \; K_{34} = \frac{K}{X_3 + X_4}$$

where $K = 1.5 V_n^2 \omega_0 / S_{\text{base}}$.

H_G is the SG inertia constant, and D_G is the load damping. R_G and T_G are droop coefficient and the speed governor time constant. F_{HP}, T_{RH} and T_{CH} denote coefficients of the reheat turbine. The system data are presented in Table VI.

To demonstrate the VSGs output power decoupling, the SG is first assumed to have an infinite inertia that its frequency is constant, i.e., $\Delta\omega_4 = 0$. $\Delta P_2/\Delta P_1^*$ is derived from Fig. 16, and its frequency response is shown in Fig. 17. Taking -10 dB as a threshold, the methods in [17], [19] and [22] still enable a passband; however, the proposed method limits the interaction well, and a better oscillation attenuation can be achieved.

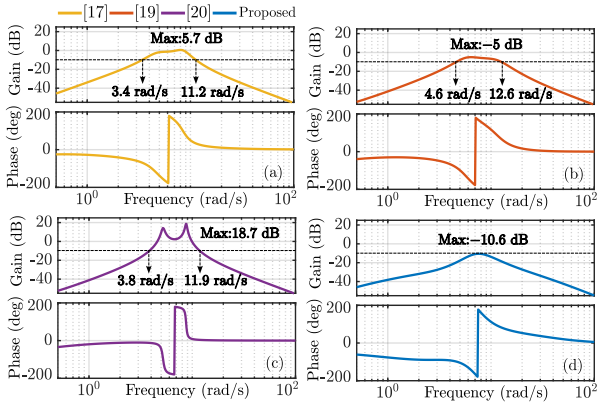

Figure 17. $\Delta P_2/\Delta P_1^*$ bode plot. (a) With the method in [17]; (b) With the method in [19]; (c) With the method in [22]; (d) With the proposed method

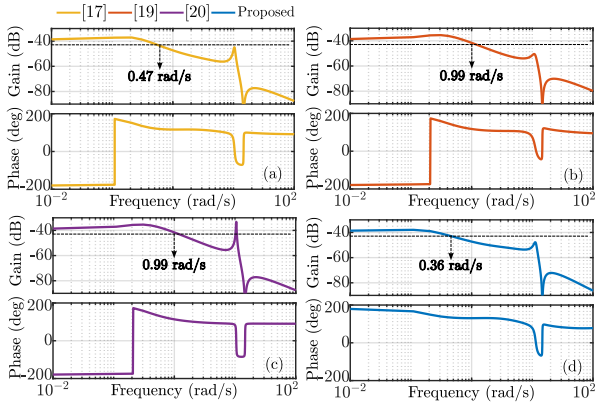

Figure 18. $\Delta\omega_{m1}/\Delta P_L$ bode plot. (a) With the method in [17]; (b) With the method in [19]; (c) With the method in [22]; (d) With the proposed method

Afterwards, assuming that $\Delta\omega_4$ is governed by the SG, the power-frequency dynamic assessment is applied by analyzing $\Delta\omega_{m1}/\Delta P_L$. The frequency response of $\Delta\omega_{m1}/\Delta P_L$ is first shown in Fig. 18. Under the identical operating condition, the proposed method can limit the $\Delta\omega_{m1}/\Delta P_L$ cutoff frequency better than the others. Correspondingly, under 0.1 p.u. load change, as the frequency trajectory depicted in Fig. 19, the proposed method provides a better inertial response to limit the rate of change of frequency and frequency nadir, which is a desirable feature for the system frequency stability.

D. Experimental Validation

A scale-down experimental validation is then applied. The test setup is illustrated in Fig. 20, where three 2.2 kW Danfoss

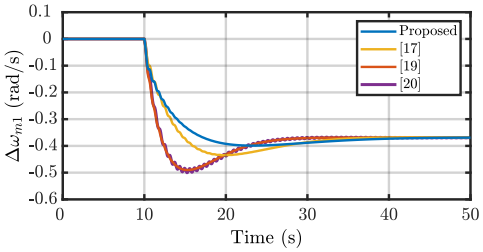

Figure 19. System frequency trajectory under 0.1 p.u. load change.

Table VII
THE PARAMETERS USED IN THE EXPERIMENT

Symbol	Values	Symbol	Values	Symbol	Values
S_{base}	2.2 kW	V_{line}	220 V	R_{fn}	0.005 p.u.
L_{fn}	0.077 p.u.	C_{fn}	16.08 p.u.	R_{ln}	0.005 p.u.
L_{ln}	0.051 p.u.	R_g	0.018 p.u.	L_g	0.036 p.u.
l_{pn}	0.14 p.u.	l_{in}	9.09 p.u.	k_{pn}	7.7 p.u.
k_{in}	1320 p.u.	R_{vn}	0 p.u.	X_{vn}	0 p.u.
T_c	100 μs	H_n	5 s	D_n	10 p.u.
m_{pn}	0.5 p.u.	m_{in}	0.25 p.u.	V_0	180 V
ω_{dn}	19 rad/s	k_{sn}	0.77	T_{sn}	3.89
ω_r	19 rad/s	T_m	0.21	k_{mn}	0.17

inverters are used for implementing multiple grid-tied VSGs, and the controllers are realized via dSPACE DS1006. Chroma 61845 is used to simulate the grid. The grid-side current and VSG output power are recorded by the oscilloscope. The parameters used in the experiment are listed in Table VII. In the experiment, the power set point change ($\Delta P_n^* = 0.2$ p.u.), grid frequency variation ($\Delta f_g = -0.1$ Hz), and grid voltage dip ($V_{\text{line}} = 0.8$ p.u.) are applied to test the proposed method.

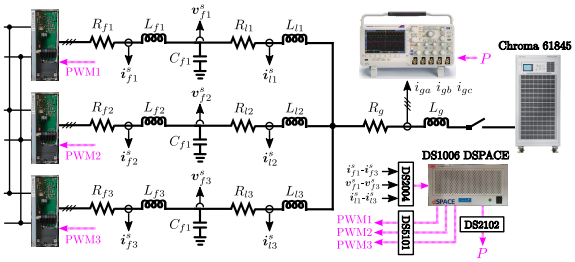

Figure 20. Experimental setup.

1) Power set point variation: As shown in Fig. 21 (a), when multiple grid-tied VSGs are poorly damped, the output power inevitably oscillates when the set point is changed, and the oscillation which is caused by the interaction among VSGs is obvious. Meanwhile, the grid-side current gets distorted, which degrades the power quality and increases the risk of instability. As a comparison, when the proposed active-damping method is applied, both self- and mutually induced oscillations are suppressed remarkably, and the set point tracking is reached within 50 ms. Only slight variations are left, and the impact of them is negligible.

2) Grid frequency variation: Under a grid frequency variation ($\Delta f_g = -0.1$ Hz), it can be seen in Fig. 22 (a) that the grid-side current and VSG output power contain sustained oscillations at a frequency of 16 rad/s. Roughly, the oscillations sustain for 4 s. By comparison, with the proposed active-damping method, the power oscillations are

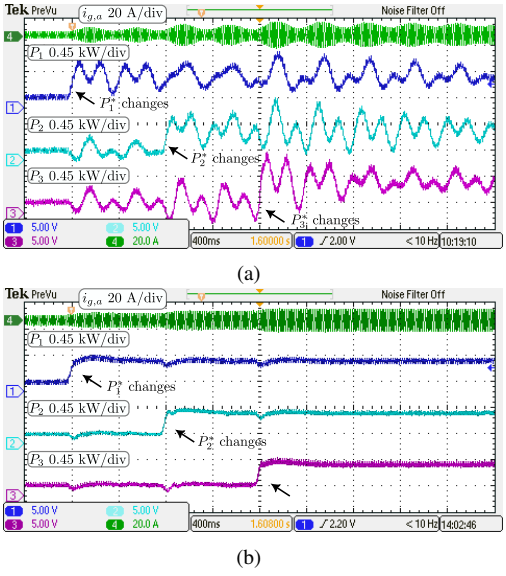

Figure 21. Waveform under the set point changes ($\Delta P_n^* = -0.2$ p.u.). (a) Without the proposed algorithm; (b) With the proposed algorithm.

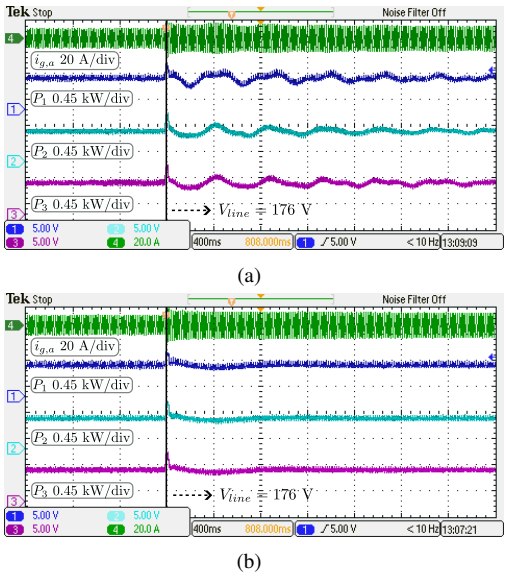

Figure 23. Waveform under the voltage dip (V_{line}=176 V). (a) without the proposed algorithm; (b) with the proposed algorithm.

fully eliminated, and only the inertial response is left. Clearly, after reaching the peak output of 0.63 kW, the active power decreases to the steady output of 0.23 kW without oscillations.

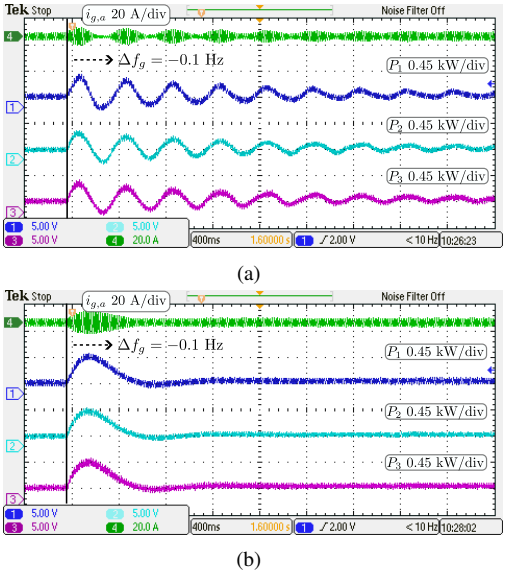

Figure 22. Waveform under the frequency change ($\Delta f_g = -0.1$ Hz). (a) Without the proposed algorithm; (b) With the proposed algorithm.

3) Symmetrical grid voltage dip: As shown in Fig. 23 (a), under a voltage dip ($V_{\text{line}} = 176$ V), VSGs are still able to remain the synchronism, and the grid-side current increases to deliver the same amount of power. Without the proposed active-damping method, output power contains oscillations that sustain for around 2.8 s, and they are attenuated by the proposed method. As shown in Fig. 23 (b), under the same disturbance, the power output is almost unaffected.

V. Discussion

The proposed active-damping method is developed on the basis of an equivalent grid model for attenuating the low-frequency oscillations that come from the parallel operation of multiple grid-tied VSGs. In this sense, the proposed method mainly contributes to the low-frequency oscillation damping within multiple grid-tied VSGs, e.g., an VSG-based power plant. Therefore, in the case of disturbances like short-circuit faults, especially considering different types of faults, short-circuit levels, and fault points, additional algorithms need to be developed and integrated to deal with the potential wide-band oscillations that may happen in the electrical network.

VI. Conclusion

In this paper, an active-damping control method is proposed to attenuate both self- and mutually induced low-frequency power oscillations in multiple grid-tied VSGs. The eigenvalue analysis indicates that the parallel operation of multiple grid-tied VSGs may lead to a low damping ratio of the dominant modes. An active-damping control with both self- and mutual-damping controllers is developed. Applying the self-damping controller, the self-induced power oscillations are attenuated. With the mutual-damping controller, VSGs output powers are further improved with almost no interactions. Moreover, the preferable inertial response is enhanced. For the practical implementation, control parameter tuning criteria are presented. Considering the parallel operation of multiple VSGs inevitably involves system setting variations, an online automatic tuning algorithm is proposed to adapt to the changes. Using the eigenvalue analyses, simulations and experiments, the effectiveness of the proposed method has been validated.

The investigation on the active-damping of multiple VSGs in parallel can be further expanded in the following aspects: i) removing the need for communication to reduce the complexity of the control implementation; ii) considering the operation under fault conditions, for instance, the transient stability, over current prevention and damping of wide-band oscillations; iii) considering the complexity of the external network.

REFERENCES

[1] J. Matevosyan *et al.*, "Grid-forming inverters: Are they the key for high renewable penetration?" *IEEE Power and Energy Magazine*, vol. 17, no. 6, pp. 89–98, Nov. 2019.

[2] Q. Zhong and G. Weiss, "Synchronverters: Inverters that mimic synchronous generators," *IEEE Trans. Ind. Electron.*, vol. 58, no. 4, pp. 1259–1267, Apr. 2011.

[3] H. Wu *et al.*, "Small-signal modeling and parameters design for virtual synchronous generators," *IEEE Trans. Ind. Electron.*, vol. 63, no. 7, p. 4292–4303, Jul. 2016.

[4] L. Huang, H. Xin, and Z. Wang, "Damping low-frequency oscillations through VSC-HVdc stations operated as virtual synchronous machines," *IEEE Trans. Power Electron.*, vol. 34, no. 6, pp. 5803–5818, Jun. 2019.

[5] S. Dong and Y. C. Chen, "Adjusting synchronverter dynamic response speed via damping correction loop," *IEEE Trans. Power Electron.*, vol. 32, no. 2, pp. 608–619, Jun. 2017.

[6] J. Liu, Y. Miura, and T. Ise, "Fixed-parameter damping methods of virtual synchronous generator control using state feedback," *IEEE Access*, vol. 7, pp. 99 177–99 190, Jul. 2019.

[7] Y. Yang *et al.*, "A new virtual inductance control method for frequency stabilization of grid forming virtual synchronous generators," *IEEE Trans. Ind. Electron.*, vol. 70, no. 1, pp. 441–451, Jan. 2022.

[8] X. Meng, J. Liu, and Z. Liu, "A generalized droop control for grid-supporting inverter based on comparison between traditional droop control and virtual synchronous generator control," *IEEE Trans. Power Electron.*, vol. 34, no. 6, pp. 5416–5438, Jun. 2019.

[9] D. B. Rathnayake, R. Razzaghi, and B. Bahrani, "Generalized virtual synchronous generator control design for renewable power systems," *IEEE Trans. Sustain. Energy*, vol. 13, no. 2, pp. 1021–1036, Apr. 2022.

[10] Y. Yu *et al.*, "A reference-feed-forward-based damping method for virtual synchronous generator control," *IEEE Trans. Power Electron.*, vol. 37, no. 7, pp. 7566–7571, Jul. 2022.

[11] J. Alipoor, Y. Miura, and T. Ise, "Power system stabilization using virtual synchronous generator with alternating moment of inertia," *IEEE J. Emerg. Sel. Topics Power Electron.*, vol. 3, no. 2, pp. 451–458, Jun. 2015.

[12] D. Li, Q. Zhu, S. Lin, and X. Y. Bian, "A self-adaptive inertia and damping combination control of VSG to support frequency stability," *IEEE Trans. Energy Convers.*, vol. 32, no. 1, pp. 397–398, Mar. 2017.

[13] F. Wang, L. Zhang, X. Feng, and H. Guo, "An adaptive control strategy for virtual synchronous generator," *IEEE Trans. Ind. Appl.*, vol. 54, no. 5, pp. 5124–5133, Sept. 2018.

[14] Z. Wang, Y. Yu, W. Gao, M. Davari, and C. Deng, "Adaptive, optimal, virtual synchronous generator control of three-phase grid-connected inverters under different grid conditions—an adaptive dynamic programming approach," *IEEE Trans. Ind. Inform.*, vol. 18, no. 11, pp. 7388–7399, Nov. 2022.

[15] J. Alipoor, Y. Miura, and T. Ise, "Stability assessment and optimization methods for microgrid with multiple VSG units," *IEEE Trans. Smart Grid*, vol. 9, no. 2, pp. 1462–1471, Mar. 2018.

[16] M. Chen, D. Zhou, C. Wu, and F. Blaabjerg, "Characteristics of parallel inverters applying virtual synchronous generator control," *IEEE Trans. Smart Grid*, vol. 12, no. 6, pp. 4690–4701, Nov. 2021.

[17] Z. Shuai, W. Huang, Z. J. Shen, A. Luo, and Z. Tian, "Active power oscillation and suppression techniques between two parallel synchronverters during load fluctuations," *IEEE Trans. Power Electron.*, vol. 35, no. 4, pp. 4127–4142, Apr. 2020.

[18] M. Chen, D. Zhou, and F. Blaabjerg, "Active power oscillation damping based on acceleration control in paralleled virtual synchronous generators system," *IEEE Trans. Power Electron.*, vol. 36, no. 8, pp. 9501–9510, Aug. 2021.

[19] S. Fu *et al.*, "Power oscillation suppression of multi-VSG grid via decentralized mutual damping control," *IEEE Trans. Ind. Electron.*, vol. 69, no. 10, pp. 10 202–10 214, Oct. 2022.

[20] S. Fu *et al.*, "Power oscillation suppression in multi-VSG grid by adaptive virtual impedance control," *IEEE Syst. J.*, vol. 16, no. 3, pp. 4744–4755, Sept. 2022.

[21] B. Qin, Y. Xu, C. Yuan, and J. Jia, "A unified method of frequency oscillation characteristic analysis for multi-VSG grid-connected system," *IEEE Trans. Power Del.*, vol. 37, no. 1, pp. 279–289, Feb. 2022.

[22] P. Sun, J. Yao, Y. Zhao, X. Fang, and J. Cao, "Stability assessment and damping optimization control of multiple grid-connected virtual synchronous generators," *IEEE Trans. Energy Convers.*, vol. 36, no. 4, pp. 3555–3567, Dec. 2021.

[23] A. Gonzalez-Cajigas, J. Roldan-Perez, and E. J. Bueno, "Design and analysis of parallel-connected grid-forming virtual synchronous machines for island and grid-connected applications," *IEEE Trans. Power Electron.*, vol. 37, no. 5, pp. 5107–5121, May 2022.

Yun Yu Yun Yu received the B.S. degree from the China University of Mining and Technology, Xuzhou, China, in 2016, and the M.S. degree from the Tianjin University, Tianjin, China, in 2019, both in electrical engineering. He is currently working toward the Ph.D. degree at AAU Energy, Aalborg University, Aalborg, Denmark.

His research interests include modelling, stability, and control of power electronic-based systems.

Sanjay K. Chaudhary received the M.Tech. degree in electrical engineering from IIT Kanpur, Kanpur, India, in 2002, and the Ph.D. degree in electrical engineering from Aalborg University, Aalborg, Denmark, in 2011. He was with ABB Ltd., Bengaluru, India, from 2002 to 2005, and then he joined Honeywell Technology Solutions Laboratory, Bengaluru.

Since 2011, he has been an Assistant Professor with AAU Energy, Aalborg University, Aalborg, Denmark.

Gibran David Agundis Tinajero received the B.S. degree in mechanical and electrical engineering and the M.Sc. and Ph.D. degrees in electrical engineering from the Universidad Autónoma de San Luis Potosí, San Luis Potosí, Mexico, in 2012, 2014, and 2018, respectively. He is currently working as a Postdoctoral Fellow with AAU Energy, Aalborg University, Aalborg, Denmark.

His research interests include modeling, analysis, and control of microgrid clusters.

Luona Xu received the B.S. degree in Electrical Engineering and Automation from China Agricultural University, Beijing, China, in 2014, and M.S. degree in Electrical Engineering from University of Chinese Academy of Sciences, Beijing, China, in 2017. From 2017 to 2019, she was an electrical engineer in East China Electric Power Design Institute Co., Ltd., Shanghai, China. She is currently working toward the Ph.D. degree at AAU Energy, Aalborg University, Denmark.

Her research interests include coordinated control for shipboard microgirds and pulsed load power supply.

Juan C. Vasquez received the B.S. degree in electronics engineering from the Autonomous University of Manizales, Manizales, Colombia, in 2004, and the Ph.D. degree in automatic control, robotics, and computer vision from BarcelonaTech-UPC, Barcelona, Spain, in 2009.

Since 2019, he has been a Full Professor with AAU Energy, Aalborg University, Aalborg, Denmark, where he is the Vice Program Leader of the Microgrids Research Program.

Josep M. Guerrero received the B.S. degree in telecommunications engineering, the M.S. degree in electronics engineering, and the Ph.D. degree in power electronics from the Technical University of Catalonia, Barcelona, Spain, in 1997, 2000, and 2003, respectively.

Since 2011, he has been a Full Professor with AAU Energy, Aalborg University, Aalborg, Denmark, where he is responsible for the Microgrid Research Program.